Tunable Conductive Nanoparticle Wire Arrays Fabricated by Convective Self-Assembly on Nonpatterned Substrates

Cosmin Farcau, Helena Moreira, Benoît Viallet, Jérémie Grisolia, and Laurence Ressier*

Université de Toulouse, INSA-CNRS-UPS, LPCNO, 135 avenue de Rangueil, 31077 Toulouse Cedex 4, France

ABSTRACT Ordered arrays of centimeter-long nanoparticle wires are fabricated by convective self-assembly from aqueous suspensions of 18 nm gold colloids, on flat SiO_2/Si substrates without any prepatterning. The orientation of the wires can be switched from parallel to perpendicular to the substrate—liquid—air contact line by controlling the substrate temperature. While the wires parallel to the meniscus are obtained by a stick—slip process, a mechanism based on critical density-triggered particle pinning is proposed to explain the formation of wires perpendicular to the meniscus. The geometry of the wire arrays is tuned by simply controlling the meniscus translation speed. Wires are typically characterized by widths of a few micrometers (1.8-8.2 μm), thicknesses of mono- to multilayers (18-70 nm), and spacings of few tens of micrometers. The fabricated nanoparticle wires are conductive, exhibiting a metallic resistive behavior in ambient conditions. Resistivity values of 5×10^{-6} and 5×10^{-2} Ωm are obtained on multilayer and monolayer nanoparticle wires, respectively. Such conductive nanoparticle wire arrays, fabricated by a simple and low-cost bottom-up strategy, offer opportunities for developing nanoparticle-based functional devices.

KEYWORDS: colloidal nanoparticles · convective self-assembly · conductive wires

Nanoscale metallic structures possess unique properties, mainly determined by the large surface-to-volume ratio, which make them extremely interesting for applications in several fields of science and technology.[1,2] Chemically synthesized colloidal nanoparticles have a series of advantages over lithographically prepared nanostructures: they can be easily produced in large amounts, broad range of sizes, controlled shape, with a narrow size and shape dispersion.[3,4]

While investigating the size- and shape-dependent properties of individual nano-objects is useful from a fundamental point of view,[5,6] many practical applications mainly rely on collective effects in assemblies of a large number of nanoparticles.[7] For instance, one can cite chemiresistor sensors based on changes in the electrical conductivity of gold nanoparticle films[8] or optical bio(chemo)sensors based on surface-enhanced Raman spectroscopy from arrays of noble metal nanoparticles.[9] One major challenge is thus to control the fabrication of such assemblies of colloidal nanoparticles on defined areas of surfaces in order to obtain application-specific hierarchical structures.

Convective self-assembly (CSA) is a colloidal assembly method based on particle flux toward the substrate—liquid—air contact line, caused by solvent evaporation in this area, and attractive capillary forces.[10] CSA was employed for producing mono- or multilayer particle films from a large variety of colloidal micro- and nanoparticles.[11−15] However, the assembly of small metallic colloids (<20 nm) remains rather sparsely explored in CSA, with very few reports being available.[12,15,16] In order to direct and localize the assembly of colloids, CSA has been applied on chemically or topologically patterned surfaces.[17] AFM oxidation lithography or photolithography combined with chemical functionalization,[18,19] and microcontact printing[20] have been previously used to create hydrophilic/hydrophobic patterns, while other conventional lithographic techniques[21] have been used to create relief surface patterns. Nevertheless, for many applications, the ability to fabricate regular nanoparticle patterns on chemically homogeneous and flat substrates, implying no lithographic processes, would considerably simplify device fabrication, reduce costs, and increase the flexibility on the substrate choice.

In this article, we show the capabilities of CSA to fabricate conductive wire arrays made of gold nanoparticles on flat, nonpatterned SiO_2/Si substrates. The mechanisms driving the formation of these nanoparticle wire arrays and the selection of their orientation relative to the meniscus are discussed. The evolution of the morphology

*Address correspondence to laurence.ressier@insa-toulouse.fr.

Received for review August 24, 2010 and accepted October 21, 2010.

Published online November 1, 2010.
10.1021/nn102128w

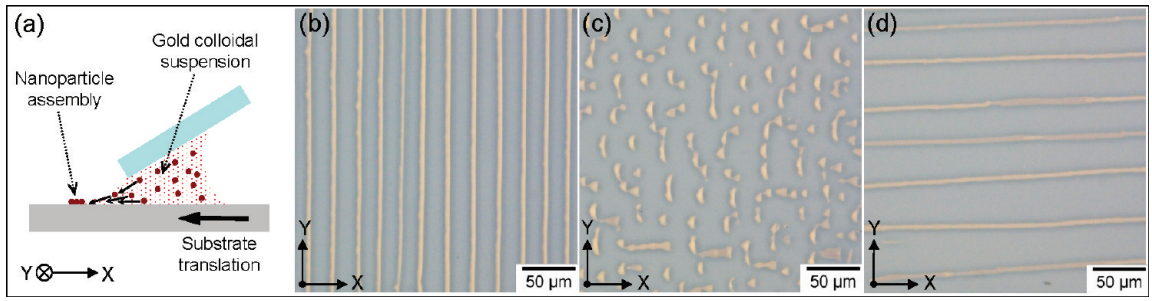

Figure 1. (a) Schematic representation of the convective self-assembly (CSA) process. The meniscus is parallel to the *Y* direction. Optical microscopy images of (b) an array of *Y*-parallel nanoparticle wires (called *Y*-type wires) obtained at T_s = 18 °C, (c) island-like nanoparticle patterns obtained at T_s = 15.5 °C, and (d) an array of *X*-parallel nanoparticle wires (called *X*-type wires) obtained at T_s = 12.5 °C. The meniscus speed *v* was kept constant at 1 μm/s during the whole experiment.

of the wire arrays with the meniscus translation speed and the substrate temperature is studied. The impact of the wire morphology on the electrical resistivity of the nanoparticle wires is quantified.

RESULTS AND DISCUSSION

Convective Self-Assembly. A schematic representation of the convective self-assembly process used to fabricate nanoparticle wire arrays is given on Figure 1a. Figure 1b shows typical optical microscopy images of an array of gold nanoparticle wires parallel to the meniscus, obtained by CSA at a meniscus speed v = 1 μm/s and a substrate temperature T_s = 18 °C. We will denote these nanoparticle wires, parallel to the meniscus, as *Y*-type wires. By decreasing the substrate temperature to 15.5 °C, the island-like patterns in Figure 1c were obtained. By further reducing the substrate temperature to T_s = 12.5 °C, a dramatic change was observed in the orientation of the wires, which had grown in this case in the direction perpendicular to the moving three-phase contact line, as seen in Figure 1d. We will denote these nanoparticle wires, perpendicular to the meniscus, as *X*-type wires.

Striped patterns parallel to the meniscus were previously obtained by convective assembly of polymer micrometer-sized colloids[22] and, more recently, of nanometer-sized gold colloids.[16,23] Similar patterns have also been obtained by removal of a substrate through a Langmuir–Blodgett monolayer.[24] The mechanism governing the formation of these *Y*-type wire arrays, parallel to the meniscus, is the "stick–slip" motion of the moving meniscus across a hydrophilic substrate.[22,25] Particles arrive toward the meniscus within the convective flux caused by evaporation in this region and are pinned to the substrate due to capillary forces and friction to the substrate. A monolayer of particles starts to deposit, and the meniscus remains further attached to the growing wire; the "stick" stage begins. The particles brought to the meniscus by convective flow are embedded into the growing wire. Meanwhile, the meniscus remains attached and starts to be elongated. When this elongation reaches a critical point, the pinning force to the wire is not able to compensate it, so the meniscus detaches and jumps to a position determined by the receding contact angle; this is the "slip" stage. The stick–slip process repeats periodically, thus a highly ordered wire array is obtained. Such deposition of colloidal particles along the meniscus is a phenomenon that has been frequently observed and discussed in the context of "coffee rings".[26]

One of the remarkable results of the present work is the switching of the wire orientation from parallel (*Y*-type wires) to perpendicular (*X*-type wires) to the moving meniscus, by decreasing the substrate temperature. In Figure 2, we present a series of optical microscopy images, capturing the essential stages of the growth of *X*-type wires and highlighting their mechanism of formation. Initially, a well-defined, straight meniscus, free of nanoparticles, is translated across the substrate (Figure 2a). Because of the aqueous solvent evaporation, nanoparticles start to accumulate slowly in the meniscus region, and this can be seen as a darkening of this region in Figure 2b. A peculiar and critical

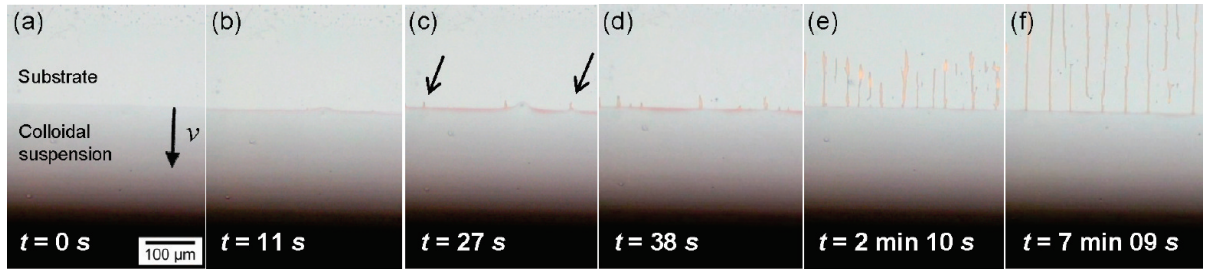

Figure 2. Series of optical microscopy images showing the time evolution of the growing of *X*-type nanoparticle wires at v = 1 μm/s and T_s = 12.5 °C. The arrows in (c) indicate the tips of wires.

aspect for the formation of *X*-type wires is the fact that nanoparticles are not deposited on the substrate at the initial stages but are dragged along with the meniscus (see the evolution from Figure 2a to c). As evaporation rates are reduced with temperature, the flux of water (and nanoparticles) in the drop toward the meniscus is lowered. Since the area and shape of the meniscus are not changed with temperature (the dependence of contact angle on temperature is negligible for water in this temperature interval), this means that the water flux is lowered, and thus also the speed of nanoparticles within. This behavior was previously confirmed and sustained by simulations of water flux during CSA.[27] The low nanoparticle momentum does not allow them to protrude the water−air interface and to get pinned to the substrate, so they remain in the liquid at the meniscus. The local nanoparticle concentration at the meniscus continues to rise slowly, which causes the increase of nanoparticle-nanoparticle and nanoparticle−substrate interactions. When a critical local density is achieved, the nanoparticles pin to the substrate, and the tip of a wire protrudes perpendicularly to the meniscus (marked by the arrows in Figure 2c). This happens at apparently random locations along the meniscus. Subsequently, other *X*-type wires start to grow in the spaces between already existing wires, specifically in the zones where the nanoparticle concentration continued to rise (see evolution from Figure 2c to 2e). Finally, the density of the growing *X*-type wires is auto-optimized in order to accommodate involved local nanoparticle densities and fluxes, and a pretty well-organized array is obtained (Figure 2f). We assume that the interwire distance d is determined by the given set of experimental conditions (substrate temperature, ambient temperature and humidity, meniscus speed, contact angle, suspension concentration) and is finally set to an optimal distance D at which two neighboring wires can grow at a steady rate. Three distinct cases can be discussed: (i) when $d > 2D$, a region will exist between the two nanoparticle wires, where the nanoparticle concentration can continue to increase, reach the critical density, and a third wire will grow; (ii) when $2D > d > D$, after the third nanoparticle wire starts to grow, the equilibrium growth of the two other wires is perturbed, and the incoming nanoparticle flux will not be enough to sustain the growth of all three wires; (iii) when $D > d$, two nanoparticle wires are too close to each other, likewise, their growth cannot reach a steady state. This interpretation is somewhat supported by Figure 2f, where it can be seen that some nanoparticle wires are interrupted; this appears to happen mostly when two wires are very close to each other.

By corroborating optical image analyses with atomic force microscopy (AFM) measurements (below), one can estimate the amount of nanoparticles deposited per unit area of the substrate. By considering a pair set of *X*-type and *Y*-type wires prepared with $v = 1$ μm/s, we estimated that the rate of particle deposition is more than 5 times lower in the case of *X*-type wires than for the *Y*-type wires. This is consistent with the lowered evaporation rates invoked above in our explanation of the mechanism of *X*-type wire formation. Some other effects caused by the temperature gradients across the droplet, and which could influence the assembling process, are the nonhomogeneous evaporation rates and the Marangoni effect.[28] Since the main effect of decreasing the substrate temperature is to reduce the solvent evaporation rate, we can expect that similar results would be obtained by controlling the humidity and ambient temperature. Controlling the substrate temperature, as in this work, seems anyway more practical and easier to implement.

Arrays of wires perpendicular to the meniscus have not been previously obtained by CSA, to our knowledge. Such arrays of nanoparticle wires have only been fabricated by another more complex technique, namely, by vertical pulling of a substrate through a Langmuir−Blodgett colloidal monolayer,[29] and from colloids dispersed in an organic solvent. Another report[30] showed the formation of both concentric rings (parallel to the meniscus) and radial spokes (perpendicular to the meniscus) by evaporation of a toluene drop containing quantum dots in a sphere on flat confined geometry. The two types of nanoparticle patterns were obtained in the same experiment, during which the temperature was not changed. In both refs 29 and 30, the formation of wire arrays perpendicular to the meniscus was ascribed to the so-called "fingering instability" of the drying front.[31,32] While our *X*-type wires are similar, to some extent, to those in ref 29, their growing behaviors are rather contrasting because, in our case, the nanoparticle wires start to grow one at a time. Furthermore, in our experiments, the meniscus remained straight and uniform during its translation. This contrasts with the macroscopically visible deformations and slips of the contact line and fingering patterns appearing some distance behind the dewetting front, observed with fingering instability.[32] With this argument, and in strength of the observations described above (Figure 2) on the formation of *X*-type wires, we believe that fingering instabilities do not play a crucial role in the growth of the *X*-type nanoparticle wires. Instead, nanoparticle−substrate pinning is triggered when the nanoparticle density at the meniscus locally reaches a critical value.

Finally, the island-like nanoparticle patterns obtained in the intermediate state (Figure 1c), appear to be due to a competition between the two mechanisms governing the formation of *Y*- and *X*-type wires.

Morphology. Figure 3 presents some typical AFM observations of the fabricated nanoparticle wires, with *Y*-type wires in Figure 3a−c and *X*-type wires in Figure 3d−f. The thickness of each *Y*-type wire is always asymmetrically distributed, starting from 18 nm (ie a mono-

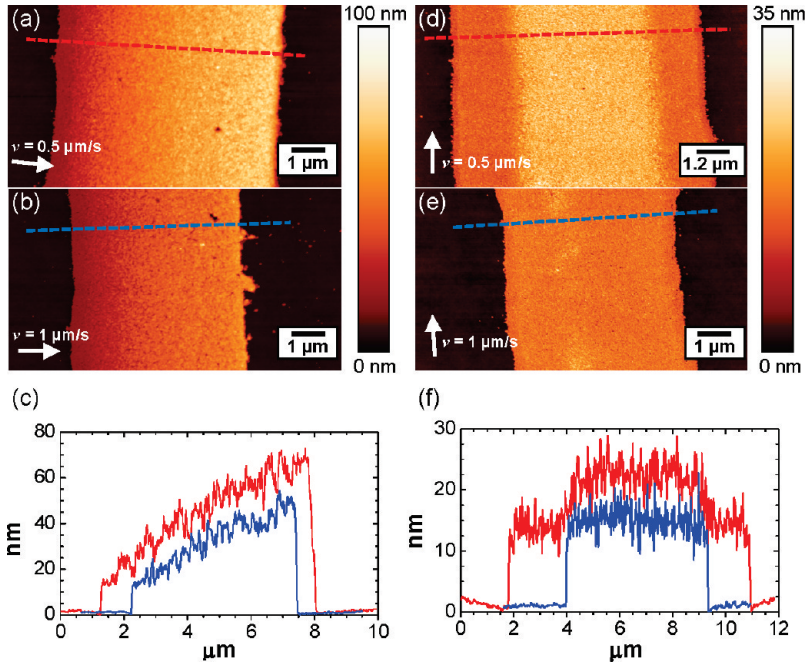

Figure 3. (a,b) AFM top views of *Y*-type wires, (c) cross sections through the *Y*-type wires marked in (a) and (b). (d,e) AFM top views of *X*-type wires, (f) cross sections through the *X*-type wires marked in (d) and (e). The arrows indicate the direction of meniscus translation during the CSA process.

layer of nanoparticles) on one side (on the left in Figure 3a−c) and increasing in steps up to 70 nm, for the largest wires, on the opposite side. The asymmetry in the *Y*-type wires is related to the direction of meniscus movement and the mechanism of the wire growth. The thicker side is always facing the suspension droplet. On the contrary, the *X*-type wires are always symmetric, being either monolayers (as in Figure 3e) or bilayers (as in Figure 3d). In bilayer wires, the top layer is narrower and centered above the base layer (see Figure 3d,f). Since *X*-type wires are perpendicular to the moving meniscus, the nanoparticle flux created by convective flow toward the growing end of the wire is symmetrically distributed with respect to the mirror plane containing the axis of the wire.

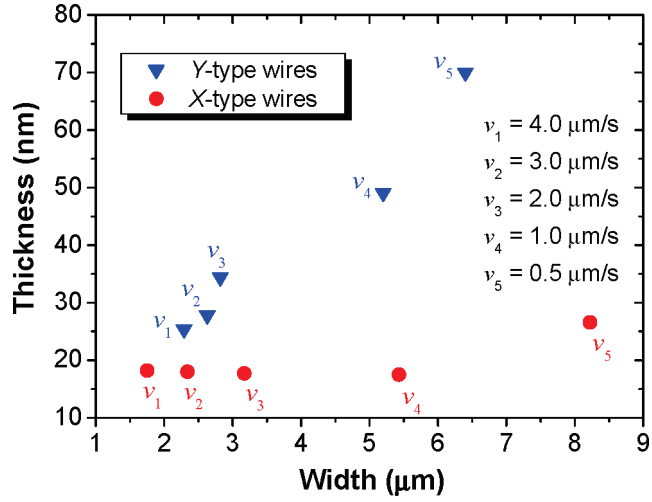

Figure 4. Wire thickness *vs* width as function of the meniscus speed *v*, for both *Y*- (blue triangles) and *X*-type (red circles) wires. The substrate temperature was 18 °C for *Y*-type wires and 12.5 °C for *X*-type wires.

Besides controlling the orientation and axial symmetry of the nanoparticle wires, a fine-tuning of their width and thickness was achieved by controlling the meniscus translation speed. Figure 4 summarizes the results obtained by modifying the meniscus speed from 0.5 to 4 μm/s for both types of nanoparticle wires. Interestingly, the wire width dependence on meniscus speed follows a similar trend for the two types of nanoparticle wires, with widths of 2.3 and 1.8 μm at the highest speed and up to 6.4 and 8.2 μm at the lowest speed, for the *Y*- and *X*-type wires respectively.

On the contrary, the thickness of the *Y*-type wires increases rapidly by decreasing the meniscus speed, while that of *X*-type wires increases very slowly. At the highest speed (4 μm/s), the *Y*-type wires have a bilayer structure, while the *X*-type wires are completely formed by a monolayer of particles. The monolayer thickness (18 nm) is in good agreement with the nanoparticle sizes measured by transmission electron microscopy. Curiously, the bilayer thickness (~28 nm) is smaller than a theoretical value (32 nm) estimated by pure geometrical considerations. At the lowest meniscus speed (0.5 μm/s), the thickness of the *Y*-type wires reaches 70 nm, which could correspond to approximately 5−6 nanoparticle layers, while the *X*-type wires barely reach the bilayer thickness (28 nm).

Figure 5 presents typical scanning electron microscopy (SEM) micrographs of a *Y*-type wire. A loosely packed assembly, with cracks and voids, is observed all across the wire width. One can identify two different length scales on which these packing defects span: the long-range order is clearly broken by the wide (10−30 nm), easily visible cracks, which appear to penetrate from the top to the bottom of the nanoparticle wire, reaching the substrate; then, the short-range order is distorted from the close-packed hexagonal lattice, due to the size dispersion (~15%) of the gold nanoparticles. At a first look, the cracks (Figure 5c) appear similar to those often observed in thick colloidal crystals,[33] where the drying stage was identified as a cause. Solvent can be trapped between the nanoparticles during the wire growth, and its subsequent evaporation can induce cracks. Moreover, we suspect that aggregates are formed near the meniscus due to the increased concentration of nanoparticles induced by the CSA process. Such aggregates would then be integrated in the growing wire. In fact, some preliminary experiments on CSA at higher substrate temperatures (20−22 °C) led to the

observation of isolated nanoparticle aggregates in the space between the *Y*-type wires. The mechanism of cluster formation is beyond the purpose of this paper and needs further investigations. Note that the same types of packing defects were observed on both *Y*- and *X*-type wires and independently of experimental conditions (various v and T_s values). Typical SEM micrographs of an *X*-type wire are available in the Supporting Information.

A crucial point for the development of applications is the substantial length of these nanoparticle wires which can reach centimeters. The success in obtaining very long and homogeneous wire arrays strongly depends on the stability and homogeneity of the CSA deposition system; temperature heterogeneity, air currents, humidity variations, and vibrations can hamper the fabrication. Another source of heterogeneity is the variation of the nanoparticle concentration in the suspension drop during the experiment. Our samples generally contain 1 cm long *Y*-type wires, with this length being dictated by the size of our substrates. Note, however, that for the case of *X*-type wires this length is harder to obtain, due to the mentioned difficulties in maintaining unchanged experimental conditions over long time scales.

Another notable result of this work is that the prepared gold nanoparticle wires are arranged in a regular array (Figure 1b,d). The *Y*-type wire arrays are highly ordered because their growth is dictated by the stick−slip motion, which is periodically repeated. For the highest meniscus speed, the obtained period is between 18 and 19 μm, while for the lowest speed, the period is about 25−26 μm. However, the period cannot be adjusted independently of the other wire parameters. This is, in fact, inherent to the stick−slip mechanism of formation of the nanoparticle wires. By decreasing the meniscus speed, the stick time is increased, and this increases also the width and thickness of the nanoparticle wires. When a thicker wire is formed, the pinning force of the meniscus is also larger, which will allow the liquid film to elongate more during the stick stage. Consequently, after the depinning moment, the triple contact line has to move a longer distance in order to find its equilibrium position, thus the slip stage, and distance to the next wire will be larger. Therefore, a modification of the *Y*-type wire array period is always accompanied by a modification of the wire geometry. The *X*-type wires are also regularly arranged, although in this case a lower degree of ordering is attained. The growth mechanism plays again a key role in establishing the period of the array. As we have pointed out, the *X*-type wires start to grow one at a time when the local nanoparticle density at the meniscus reaches a critical value. The ordering is achieved subsequently, as a consequence of an autooptimization process, with the nanoparticles arriving at the meniscus by convective flow having the role to maintain constant the growth rate of wires. Thus, the main effect of modifying the meniscus speed is to modify the geometry of the *X*-type wires, and their period remains in the rather broad interval of 35−50 μm. In both *Y*- and *X*-type wires, the extensions of the array in the direction perpendicular to the wires can also reach centimeters. For *Y*-type wires, this parameter is determined by the distance on which the meniscus is translated, while for *X*-type wires, it is determined by the lateral dimensions of the substrate.

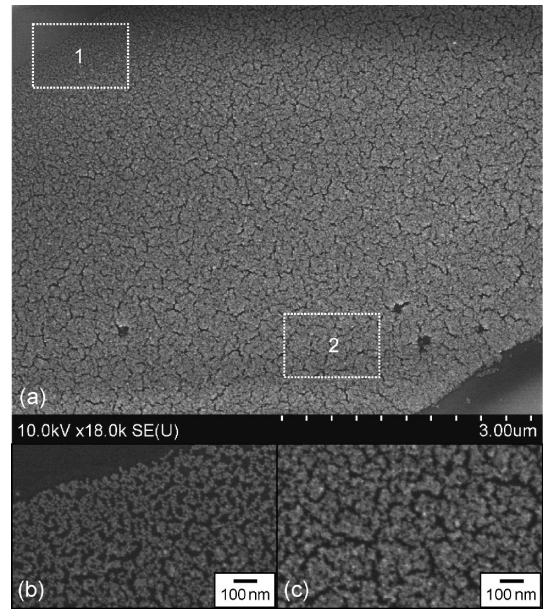

Figure 5. (a) SEM micrograph of a *Y*-type nanoparticle wire. (b,c) SEM zoomed-in images marked in (a) by rectangles (1) and (2), respectively, showing the nanoparticle packing on the thin side and the thick side of the nanoparticle wire (see also Figure 3c).

Note that although this study was focused on SiO_2/Si substrates and gold colloids, the proposed techniques could be generalized to other types of substrates and colloids. As preliminary results, we have already obtained similar arrays of gold or silica nanoparticle wires on polyethylene terephthalate and cyclo-olefin polymer flexible substrates.

Electrical Properties. As seen in the above paragraphs, arrays of gold nanoparticle wires of different geometrical parameters can be obtained during CSA by varying the meniscus translation speed and by changing the substrate temperature. Notably, adjustment of these parameters allows obtaining wire cross-sectional areas that vary within 1 order of magnitude, from 3.5×10^{-2} to 45×10^{-2} μm^2. Therefore, one could expect that this will allow tuning the electrical resistance of the wires.

To verify this idea, we performed electrical conductivity measurements at room temperature on selected samples possessing strongly contrasting morphologies: multilayer *Y*-type wires (T_s = 18 °C and v = 0.5 μm/s) and monolayer *X*-type wires (T_s = 12.5 °C and v = 1 μm/s). The typical configuration of the wire arrays connected by gold electrodes is shown in Figure 6a. In

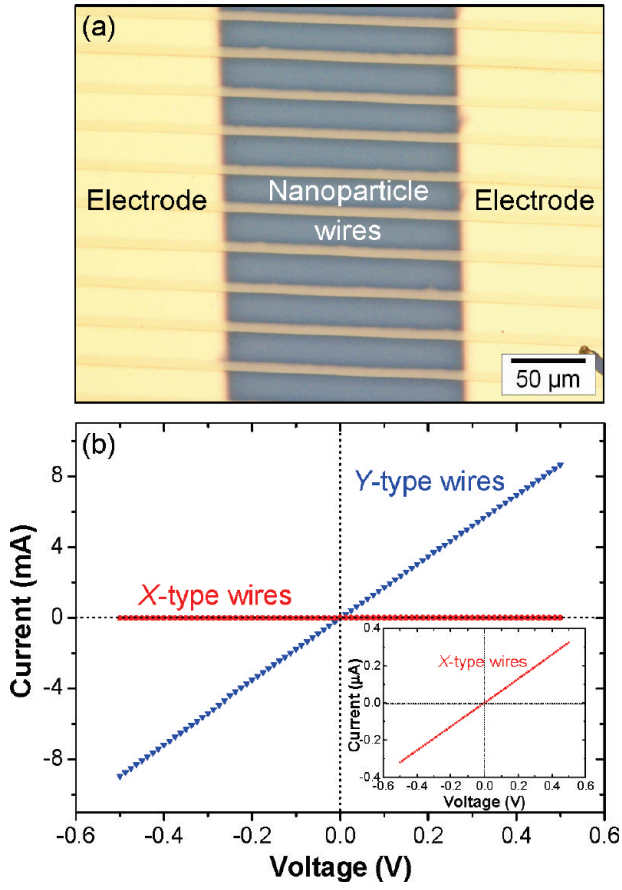

Figure 6. (a) Optical microscopy image showing the typical configuration of electrodes connecting an array of nanoparticle wires. (b) Current *vs* voltage curves at room temperature for multilayer *Y*-type (blue) and monolayer *X*-type (red) wire arrays. The inset shows the current *vs* voltage curve for the *X*-type wires, with an appropriate current scale.

both types of wires, the current follows a characteristic Ohmic behavior, as seen in the current *versus* voltage curves in Figure 6b.

In the case of *Y*-type wires, a current of about 8.7 mA (at 500 mV) was measured, which corresponds to a resistance R_Y on the order of 57 Ω. Remarkably, in the *X*-type wires, the current is 5 orders of magnitude lower (0.3 μA at 500 mV; inset in Figure 6b) than in the *Y*-type, which yields a resistance R_X of 1.5 MΩ. Control measurements on substrates without nanoparticles gave no detectable current (<1 pA) up to ±1 V. Since the wire array acts as a set of parallel-connected resistances, the measured overall resistances, R_Y and R_X, are determined by the number of wires *N*, their length *L*, and cross-sectional areas *A*. The typical number of connected wires is 50−80, with electrode gaps in the range of 150−200 μm, and average cross-sectional areas of 35×10^{-2} and 8×10^{-2} μm² for *Y*- and *X*-type wires, respectively. The resistivity was estimated by $\rho = RNA/L$, and values of $\rho_Y \sim 5 \times 10^{-6}$ Ωm and $\rho_X \sim 5 \times 10^{-2}$ Ωm for *Y*- and *X*-type wires, respectively, were obtained. The attained ρ_Y resistivity is only 2 orders of magnitude larger than that of bulk gold ($\sim 2.3 \times 10^{-8}$ Ωm). This indicates that a very low tunneling barrier exists between gold nanoparticles, due to the presence of some citrate ions. As far as we know, few works report the same order of resistivity for nanoparticle wires a few micrometers wide.[34] In ref 35, a resistivity of $10^{-5}-10^{-6}$ Ωm was attained with wires of a much larger cross section (100 μm × 100 nm). On gold nanoparticle monolayer assemblies similar to our *X*-type wires, a resistivity of 2×10^{-1} Ωm, which falls in the range of our ρ_X, has been previously observed, but under UHV conditions.[23]

In our samples, both *Y*- and *X*-type wires are formed by the same gold nanoparticles separated by a citrate ligand dielectric medium and deposited on a 1 μm insulator SiO_2 layer. Then, at ambient conditions, electrical transport across the assembly results mainly from the thermal activation energy of the charge carriers and the current percolation paths defined by the disorder of the assembly. The observed 4-order difference in resistivity between *Y*- and *X*-type wires could be most probably ascribed to the dimensionality of each type of wires (2D or 3D) and the defects in the nanoparticle assemblies. Previous experiments with highly ordered nanoparticle arrays indicate that the conductance in multilayers is several orders of magnitude larger than in monolayers.[36,37] A strong interlayer coupling was proposed to account for the observed differences. Additionally, it was shown that the percolation of current paths can be relevant for the overall transport behavior in nanoparticle assemblies.[38,39] In these papers, the difference in number of percolation paths is generated by Coulomb blockade-mediated tunneling. However, in our study, the difference in number of percolation paths is only due to geometrical difference: the measured *X*-type wires are predominantly monolayers, in contrast with the *Y*-type wires that possess a multilayered morphology. Furthermore, the loose-packing observed by SEM (Figure 5) could play a more drastic role in reducing the density of available current paths in the *X*-type wires than in the *Y*-type wires. Thus, more current paths can be expected in the 3D *Y*-type wires than in the 2D *X*-type wires, which can explain the 4-order magnitude difference of resistivity between *X*-type and *Y*-type wires. In fact, given the high degree of disorder observed in the SEM images (Figure 5), it is rather surprising that both types of nanoparticle wires exhibit a metallic behavior, even if the resistivity of the *X*-type wires is 6 orders of magnitude larger than that of bulk gold. This observation can have a strong impact on practical applications: a highly ordered and compact nanoparticle packing does not appear to be a strict requirement for fabricating conductive nanoparticle wires, useable for instance as interconnections in microelectronics.

CONCLUSIONS

In summary, we fabricated regular arrays of centimeter-long nanoparticle wires on a perfectly flat, nonpatterned substrate, by CSA of 18 nm gold colloids. The array period is tens of micrometers, while the width and thickness of the wires are tuned on the micrometer and nanometer scales, respectively, by controlling the meniscus translation speed. Notably, we demonstrated that the orientation of the wires parallel to the meniscus (*Y*-type wires), resulting from a known stick−slip process, can be switched to perpendicular to the meniscus (*X*-type wires) by decreasing the substrate temperature. Real-time observations of the meniscus dynamics during the growth of *X*-type wires led us to propose a previously not discussed mechanism of formation. The decrease of the substrate temperature reduces solvent convective flow, thus nanoparticles move toward the meniscus with a lowered momentum. As a consequence, they cannot protrude the water−air interface and are not pinned to the substrate, causing the increase of the nanoparticle concentration at the meniscus. When a critical local density is achieved, the nanoparticle−substrate pinning is triggered, and the tip of a wire protrudes perpendicularly to the meniscus. The event is stepwisely multiplied, and a well-organized *X*-type wire array is obtained. These observations could be fundamental for further understanding of meniscus-mediated self-assembly of nanoparticles.

The fabricated nanoparticle wires exhibit a metallic resistive behavior in ambient conditions. Despite the organization defects evidenced by SEM, resistivity values of 5×10^{-6} and 5×10^{-2} Ωm for multilayer and monolayer nanoparticle wires, respectively, are obtained.

Such tunable conductive wire arrays offer new opportunities for developing nanoparticle-based applications, such as sensors for chemical or biological species, electronic components, or electrical connections.[40] More generally, our results extend the current capabilities of CSA, as a low-cost bottom-up technique, for the customized patterning of nanoparticle wire arrays on large-area nonpatterned substrates.

METHODS

Synthesis of Gold Colloids. Gold colloids were synthesized in aqueous phase by the standard citrate reduction (Turkevich method[41]) as described in a previous work.[16] An average diameter of 18 nm with a standard deviation of 15% was determined by transmission electron microscopy. By the absorption spectra and Mie theory calculation, we determined the nanoparticle concentration of the colloidal suspension to be about 3×10^{12}/mL. For convective assembly described hereafter, the as-synthesized suspension was concentrated by centrifugation to 1.2×10^{13}/mL (corresponding to ~0.004% vol).

Convective Self-Assembly. Silicon wafers covered by a 1 μm thick layer of thermally grown silica (SiO_2) were used as substrates. These were cleaned with trichloroethylene and acetone, rinsed with ultra-high-quality water (18 MΩ), and dried in a stream of nitrogen followed by UV treatment (15 min) to render them hydrophilic. A low contact angle between 10 and 15° was then attained. A homemade CSA deposition system in a horizontal configuration, as previously described,[42] was used. Briefly, a glass deposition plate is placed in close vicinity (250 μm) to the substrate, at a 30° angle, and a droplet (20 μL) of gold colloids is injected into the formed wedge (see Figure 1a). The substrate is fixed on a copper plate, by which the temperature T_s is regulated. By translating the substrate, the meniscus formed by the colloidal suspension with the substrate can be dragged over the substrate at speeds *v* ranging from 50 nm/s to 1 mm/s. This is referred to as meniscus speed in the article. All experiments were performed in ambient air, at room temperature (23−24 °C), and a relative humidity RH = 40−45%. The setup was mounted under an Olympus BXFM optical microscope to allow real-time observations.

Morphological Characterization. The morphology of the fabricated nanoparticle wires was investigated in tapping mode by atomic force microscopy (AFM) in ambient medium using a Nanoscope IIIa Multimode scanning probe microscope from Veeco Instruments. To observe more closely the packing in the nanoparticle assemblies, we further performed scanning electron microscopy (SEM) using a Hitachi S-4800 microscope.

Electrical Measurements. The fabricated nanoparticle wires were electrically connected by gold electrodes defined by stencil lithography. The obtained electrodes were 50 nm thick with a separation of 150−200 μm. This technique was chosen in favor of conventional lithographic processes, which imply the use of resists and solvent and can contaminate the nanoparticle assembly. All DC current *versus* voltage characteristics measurements were performed in ambient conditions (23 °C, RH = 45%) with a Keithley 6430 electrometer. The bias voltage *V* was swept in the range of ±0.5 V with a rate of 10 mV/s.

Acknowledgment. This work was supported by the French National Agency (ANR) in the frame of its program "Recherche technologique Nano-INNOV/RT" (NANOCOMM Project No. ANR-09-NIRT-004).

Supporting Information Available: Lower magnification optical microscopy images of nanoparticle wires and islands, typical SEM micrographs of an *X*-type nanoparticle wire. This material is available free of charge *via* the Internet at http://pubs.acs.org.

REFERENCES AND NOTES

1. Schmid, G., Ed. *Nanoparticles: From Theory to Application*; Wiley-VCH: Weinheim, Germany, 2010.
2. Feldheim, D. L., Foss, C. A., Eds. *Metal Nanoparticles: Synthesis, Characterization, and Applications*; CRC Press: Boca Raton, FL, 2001.
3. Burda, C.; Chen, X.; Narayanan, R.; El-Sayed, M. A. Chemistry and Properties of Nanocrystals of Different Shapes. *Chem. Rev.* **2005**, *105*, 1025–1102.
4. Masala, O.; Seshadri, R. Synthesis Routes for Large Volumes of Nanoparticles. *Annu. Rev. Mater. Res.* **2004**, *34*, 41–81.
5. Trudeau, P.; Sheldon, M.; Altoe, V.; Alivisatos, A. P. Electrical Contacts to Individual Colloidal Semiconductor Nanorods. *Nano Lett.* **2008**, *8*, 1936–1939.
6. Kuemmeth, F.; Bolotin, K. I.; Shi, S.; Ralph, D. C. Measurement of Discrete Energy-Level Spectra in Individual Chemically Synthesized Gold Nanoparticles. *Nano Lett.* **2008**, *8*, 4506–4512.
7. Cheon, J.; Park, J.; Choi, J.; Jun, Y.; Kim, S.; Kim, M. G.; Kim, Y.; Kim, Y. J. Magnetic Superlattices and Their Nanoscale Phase Transition Effects. *Proc. Natl. Acad. Sci. U.S.A.* **2006**, *103*, 3023–3027.
8. Cooper, J. S.; Raguse, B.; Chow, E.; Hubble, L.; Müller, K. H.; Wieczorek, L. Gold Nanoparticle Chemiresistor Sensor Array That Differentiates between Hydrocarbon Fuels

Dissolved in Artificial Seawater. *Anal. Chem.* **2010**, *82*, 3788–3795.
9. Jones, C. L.; Bantz, K. C.; Haynes, C. L. Partition Layer-Modified Substrates for Reversible Surface-Enhanced Raman Scattering Detection of Polycyclic Aromatic Hydrocarbons. *Anal. Bioanal. Chem.* **2009**, *394*, 303–311.
10. Dimitrov, A. S.; Nagayama, K. Continuous Convective Assembling of Fine Particles into Two-Dimensional Arrays on Solid Surfaces. *Langmuir* **1996**, *12*, 1303–1311.
11. Kim, M. H.; Im, S. H.; Park, O. O. Rapid Fabrication of Two- and Three-Dimensional Colloidal Crystal Films *via* Confined Convective Assembly. *Adv. Funct. Mater.* **2005**, *15*, 1329–1335.
12. Prevo, B. G.; Fuller, J. C.; Velev, O. D. Rapid Deposition of Gold Nanoparticle Films with Controlled Thickness and Structure by Convective Assembly. *Chem. Mater.* **2005**, *17*, 28–35.
13. Lee, J. A.; Meng, L.; Norris, D. J.; Scriven, L. E.; Tsapatsis, M. Colloidal Crystal Layers of Hexagonal Nanoplates by Convective Assembly. *Langmuir* **2006**, *22*, 5217–5219.
14. Yi, D. K.; Lee, J.; Rogers, J. A.; Paik, U. Two-Dimensional Nanohybridization of Gold Nanorods and Polystyrene Colloids. *Appl. Phys. Lett.* **2009**, *94*, 084104.
15. Lee, J. A.; Reibel, K.; Snyder, M. A.; Scriven, L. E.; Tsapatsis, M. Geometric Model Describing the Banded Morphology of Particle Films Formed by Convective Assembly. *Chem. Phys. Chem.* **2009**, *10*, 2116–2122.
16. Grisolia, J.; Viallet, B.; Amiens, C.; Baster, S.; Cordan, A. S.; Leroy, Y.; Soldano, C.; Brugger, J.; Ressier, L. 99% RTS-like Noise in Gold Nanoparticles μ-Stripes. *Nanotechnology* **2009**, *20*, 489801.
17. Dziomkina, N. V.; Vancso, G. J. Colloidal Crystal Assembly on Topologically Patterned Templates. *Soft Matter* **2005**, *1*, 265.
18. Viallet, B.; Ressier, L.; Czornomaz, L.; Decorde, N. Tunable Pyramidal Assemblies of Nanoparticles by Convective/Capillary Deposition on Hydrophilic Patterns Made by AFM Oxidation Lithography. *Langmuir* **2010**, *26*, 4631–4634.
19. Fustin, C.; Glasser, G.; Spiess, H.; Jonas, U. Site-Selective Growth of Colloidal Crystals with Photonic Properties on Chemically Patterned Surfaces. *Adv. Mater.* **2003**, *15*, 1025–1028.
20. Xia, Y.; Whitesides, G. M. Soft Lithography. *Angew. Chem., Int. Ed.* **1998**, *37*, 550–575.
21. Kraus, T.; Malaquin, L.; Delamarche, E.; Schmid, H.; Spencer, N. D.; Wolf, H. Closing the Gap between Self-Assembly and Microsystems Using Self-Assembly, Transfer, and Integration of Particles. *Adv. Mater.* **2005**, *17*, 2438–2442.
22. Ray, M. A.; Kim, H.; Jia, L. Dynamic Self-Assembly of Polymer Colloids To Form Linear Patterns. *Langmuir* **2005**, *21*, 4786–4789.
23. Kakefuda, Y.; Narita, K.; Komeda, T.; Yoshimoto, S.; Hasegawa, S. Synthesis and Conductance Measurement of Periodic Arrays of Gold Nanoparticles. *Appl. Phys. Lett.* **2008**, *93*, 163103.
24. Huang, J.; Tao, A. R.; Connor, S.; He, R.; Yang, P. A General Method for Assembling Single Colloidal Particle Lines. *Nano Lett.* **2006**, *6*, 524–529.
25. Watanabe, S.; Inukai, K.; Mizuta, S.; Miyahara, M. T. Mechanism for Stripe Pattern Formation on Hydrophilic Surfaces by Using Convective Self-Assembly. *Langmuir* **2009**, *25*, 7287–7295.
26. Deegan, R. D.; Bakajin, O.; Dupont, T. F.; Huber, G.; Nagel, S. R.; Witten, T. A. Capillary Flow as the Cause of Ring Stains from Dried Liquid Drops. *Nature* **1997**, *389*, 827–829.
27. Kraus, T.; Malaquin, L.; Schmid, H.; Riess, W.; Spencer, N. D.; Wolf, H. Nanoparticle Printing with Single-Particle Resolution. *Nat. Nanotechnol.* **2007**, *2*, 570–576.
28. Hu, H.; Larson, R. G. Marangoni Effect Reverses Coffee-Ring Depositions. *J. Phys. Chem. B* **2006**, *110*, 7090–7094.
29. Huang, J.; Kim, F.; Tao, A. R.; Connor, S.; Yang, P. Spontaneous Formation of Nanoparticle Stripe Patterns through Dewetting. *Nat. Mater.* **2005**, *4*, 896–900.
30. Xu, J.; Xia, J.; Lin, Z. Evaporation-Induced Self-Assembly of Nanoparticles from a Sphere-on-Flat Geometry. *Angew. Chem., Int. Ed.* **2007**, *46*, 1860–1863.
31. Samid-Merzel, N.; Lipson, S. G.; Tannhauser, D. S. Pattern Formation in Drying Water Films. *Phys. Rev. E* **1998**, *57*, 2906.
32. Pauliac-Vaujour, E.; Stannard, A.; Martin, C. P.; Blunt, M. O.; Notingher, I.; Moriarty, P. J.; Vancea, I.; Thiele, U. Fingering Instabilities in Dewetting Nanofluids. *Phys. Rev. Lett.* **2008**, *100*, 176102.
33. Wong, S.; Kitaev, V.; Ozin, G. A. Colloidal Crystal Films: Advances in Universality and Perfection. *J. Am. Chem. Soc.* **2003**, *125*, 15589–15598.
34. Hermanson, K. D.; Lumsdon, S. O.; Williams, J. P.; Kaler, E. W.; Velev, O. D. Dielectrophoretic Assembly of Electrically Functional Microwires from Nanoparticle Suspensions. *Science* **2001**, *294*, 1082–1086.
35. Diao, J. J.; Sun, J.; Hutchison, J. B.; Reeves, M. E. Self Assembled Nanoparticle Wires by Discontinuous Vertical Colloidal Deposition. *Appl. Phys. Lett.* **2005**, *87*, 103113.
36. Muller, K.-H.; Wei, G.; Raguse, B.; Myers, J. Three-Dimensional Percolation Effect on Electrical Conductivity in Films of Metal Nanoparticles Linked by Organic Molecules. *Phys. Rev. B* **2003**, *68*, 155407.
37. Parthasarathy, R.; Lin, X.; Jaeger, H. M. Electronic Transport in Metal Nanocrystal Arrays: The Effect of Structural Disorder on Scaling Behavior. *Phys. Rev. Lett.* **2001**, *87*, 186807.
38. Blunt, M. O.; Šuvakov, M.; Pulizzi, F.; Martin, C. P.; Pauliac-Vaujour, E.; Stannard, A.; Rushforth, A. W.; Tadić, B.; Moriarty, P. Charge Transport in Cellular Nanoparticle Networks: Meandering through Nanoscale Mazes. *Nano Lett.* **2007**, *7*, 855–860.
39. Strelniker, Y. M.; Havlin, S.; Berkovits, R.; Frydman, A. Resistance Distribution in the Hopping Percolation Model. *Phys. Rev. E* **2005**, *72*, 016121.
40. Zabet-Khosousi, A.; Dhirani, A. Charge Transport in Nanoparticle Assemblies. *Chem. Rev.* **2008**, *108*, 4072–4124.
41. Turkevich, J.; Stevenson, P. C.; Hillier, J. A Study of the Nucleation and Growth Processes in the Synthesis of Colloidal Gold. *J. Discuss. Faraday Soc.* **1951**, *11*, 55–75.
42. Prevo, B. G.; Velev, O. D. Controlled, Rapid Deposition of Structured Coatings from Micro- and Nanoparticle Suspensions. *Langmuir* **2004**, *20*, 2099–2107.